Formation of an Artificial Mg^{2+}-permeable Interphase on Mg Anodes Compatible with Ether and Carbonate Electrolytes.

Yaqi Li [a,c,d], Pengjian Zuo [*,a], Ruinan Li [a], Hua Huo [a], Yulin Ma [a], Chunyu Du [a], YunZhi Gao [a], Geping Yin [**,a], Robert S. Weatherup [***,b,c,d]

a. MIIT Key Laboratory of Critical Materials Technology for New Energy Conversion and Storage, School of Chemistry and Chemical Engineering, Harbin Institute of Technology, Harbin 150001, China.
b. Department of Materials, University of Oxford, Parks Road, Oxford, OX1 3PH, UK
c. Diamond Light Source, Didcot, Oxfordshire OX11 0DE, UK
d. Research Complex at Harwell, Rutherford Appleton Laboratory, Harwell, Didcot, OX11 0FA, UK

*Corresponding author.
E-mail: zuopj@hit.edu.cn
**Corresponding author.
E-mail: yingphit@hit.edu.cn
***Corresponding author.
E-mail: robert. weatherup@materials.ox.ac.uk

Abstract

Rechargeable Mg-ion batteries typically suffer from either rapid passivation of the Mg anode or severe corrosion of the current collectors by halogens within the electrolyte, limiting their practical implementation. Here we demonstrate the broadly applicable strategy of forming an artificial solid electrolyte interphase (a-SEI) layer on Mg to address these challenges. The a-SEI layer is formed by simply soaking Mg foil in a tetraethylene glycol dimethyl ether (TEGDME) solution containing LiTFSI and $AlCl_3$, with Fourier-transform infrared and ultraviolet-visible spectroscopy measurements revealing spontaneous reaction with the Mg foil. The a-SEI is found to mitigate Mg passivation in $Mg(TFSI)_2$/DME electrolytes with symmetric cells exhibiting overpotentials that are 2 V lower compared to when the a-SEI is not present. This approach is extended to $Mg(ClO_4)_2$/DME and $Mg(TFSI)_2$/PC electrolytes, to achieve reversible Mg plating and stripping, which is not achieved with bare electrodes. The interfacial resistance of cells with a-SEI protected Mg is found to be two orders of magnitude lower than that with bare Mg in all three electrolytes, indicating the formation of an effective Mg-ion transporting interfacial structure. X-ray absorption and photoemission spectroscopy measurements show the a-SEI contains minimal $MgCO_3$, MgO, $Mg(OH)_2$ and $TFSI^-$, whilst being rich in $MgCl_2$, MgF_2 and MgS, when compared to the passivation layer formed on bare Mg.

Key words: magnesium batteries, $TFSI^-$ containing electrolyte, ether electrolyte, carbonate electrolyte, artificial SEI layer, passivation layer, X-ray Photoelectron Spectroscopy (XPS), Near-edge X-ray Absorption Fine Structure (NEXAFS)

Introduction

Magnesium metal offers a low reduction potential (2.37 V versus normal hydrogen electrode), high volumetric capacity (3,833 mA h/cm^3), and high abundance, making it attractive for low-cost, high energy density electrochemical devices.[1-3] Moreover, dendrite formation upon cycling is suppressed on account of the low barrier associated with Mg self-diffusion,[4] avoiding the safety concerns associated with internal short-circuits in rechargeable Li-metal batteries. Although the feasibility of Mg electrochemical systems was demonstrated almost two decades ago,[5] Mg-ion batteries (MIBs) still remain at the research stage. One of the main obstacles to realizing commercial MIBs is the poor compatibility between Mg metal anodes and existing electrolytes. The low reduction potential of Mg means a wide variety of solvents, salts, and contaminants are readily reduced on the metallic Mg anode forming a passivating layer that is not only electronically insulating but also typically ionically insulating, preventing reversible Mg stripping/plating.

A variety of electrolyte chemistries have been explored to improve the compatibility of Mg metal with the electrolyte, including those based on Grignard reagents,[6, 7] magnesium hexamethyldisilazide (Mg-HMDS),[8, 9] magnesium aluminum chloride complex (MACC),[10, 11] and boron-containing Mg-ion electrolytes.[12, 13] However, these typically exhibit narrow electrochemical windows or contain halogen anions (e.g. Cl^-) that may corrode metallic battery components within the charge-discharge potential window, making them unsuitable for practical devices. What's more, chlorides in the electrolyte solution are thought to hinder Mg-ion transfer between the solution phase and host lattice,[14] constraining the use of high-voltage metal oxide cathode materials in MIBs.

Amongst the halide-free electrolytes, ethereal $Mg(TFSI)_2$ (trifluoro-methane-sulfonimide [TFSI]) shows promise in avoiding current collector corrosion, whilst exhibiting a high anodic limit, high solvating power, and formation of a solvation sheath that facilitates Mg stripping/plating.[15, 16] Nevertheless, relatively low Coulombic efficiencies and large overpotentials for Mg stripping/plating are typically reported,[16] with reduction instability of $TFSI^-$ theoretically predicted[15] and experimentally observed.[17] Suppressing current collector corrosion whilst simultaneously avoiding complete passivation of the Mg surface thus remains a significant challenge in identifying electrolytes compatible with metallic Mg electrodes.

Rather than attempting to maintain a bare Mg-metal surface, the formation of a Mg-permeable solid electrolyte interphase (SEI) that avoids direct contact between the highly reducing Mg surface and the electrolyte is a broadly applicable strategy to realizing reversible Mg plating/stripping.[18] Electrolytes that are not thermodynamically stable in contact with metallic Mg, undergo reduction to form a surface layer that can be considered as either a passivation layer, if its ionic conductivity is so low that plating/striping is completely suppressed, or a SEI layer, if it exhibits low electron conductivity and high enough ionic conductivity that Mg-ions can transit under small applied potentials. Although these layers are significantly different in function, there isn't necessarily a sharp distinction between their structure and composition: Modest changes in the electrolyte composition can cause the corresponding surface layer resistance to change by orders of magnitude.[19, 20] In this direction there have thus been various attempts to engineer artificial SEI (a-SEI) layers[21] and metal-organic framework films[22] that provide Mg-ion transport but block anions and solvent molecules. A recent approach has shown that the addition of $TiCl_4$ to ethereal $Mg(TFSI)_2$ leads to formation of $Ti(TFSI)_2Cl_2$ by a ligand exchange reaction,[23] which is then thought to interact with the surface of the Mg anode to form a fresh Mg surface that facilitates reversible Mg-ion deposition and dissolution. This highlights that the chemical reaction

between electrolyte components (e.g. $TFSI^-$) and Mg compounds can be altered by other species in solution.

Herein, we introduce a simple electrode soaking approach to form an a-SEI layer that avoids passivation of Mg electrodes in a variety of MIB electrolytes including $Mg(TFSI)_2$/DME, $Mg(ClO_4)_2$/DME, and $Mg(TFSI)_2$/PC. This involves altering the decomposition of $TFSI^-$ anions on bare Mg by the addition of $AlCl_3$ to LiTFSI in TEGDME, in order to avoid the passivation behavior seen for $Mg(TFSI)_2$ on Mg. Fourier transform infrared (FTIR) and Ultraviolet-Visible (UV-vis) spectroscopy combined with scanning electron microscopy (SEM) measurements show that the chemical reaction between Mg and the solution occurs spontaneously at room temperature generating a surface layer on bare Mg. Electrochemical impedance spectroscopy (EIS) and galvanostatic discharge/charge confirms the surface layer functions as a Mg-permeable a-SEI. In an effort to clarify the difference between the a-SEI and passivation layers, specimens of Mg foil soaked in LiTFSI+$AlCl_3$/TEGDME and $Mg(TFSI)_2$/TEGDME respectively, were examined by X-ray photoelectron spectroscopy (XPS) and near edge X-ray absorption fine structure (NEXAFS) spectroscopy. The understanding developed of the differences in chemical structure between the a-SEI and passivation layers serves as a basis for further improving Mg-electrolyte interfaces for MIBs.

Methods

Materials. Anhydrous tetraethylene glycol dimethyl ether (TEGDME, 99%), ethylene glycol dimethyl ether (DME, 99.5%), lithium bis(trifluoromethanesulfonyl)imide (LiTFSI, 99%), magnesium perchlorate ($Mg(ClO_4)_2$, AR), and propylene carbonate (PC, 99.7%) were purchased from Aladdin Industrial Corporation (Shanghai). Aluminum chloride ($AlCl_3$, 98%) was purchased from Sigma-Aldrich and Magnesium(II) bis(trifluoromethanesulfonyl)imide ($Mg(TFSI)_2$, 97%) from TCI (Shanghai). All solvents were treated with 4 Å molecular sieves to remove water before use. The Mg foil surface was scraped with a sharp stainless steel blade just before use to remove the oxide film. All procedures for electrolyte synthesis, surface film preparation, battery assembly, and sample preparation were conducted in an Ar-filled glove box.

Preparation of Mg foil with a-SEI layer. 0.861 g LiTFSI was added to 5 ml TEGDME and stirred until complete dissolution, then 0.133 g $AlCl_3$ was slowly added followed by stirring for 24 hours. The scraped Mg foil was then soaked in the solution for 24 hours to yield Mg foil covered with a-SEI layer.

Preparation of Mg foil with passivation layer. A solution was prepared by adding 1.46 g $Mg(TFSI)_2$ to 5.0 ml TEGDME and stirring at room temperature for 24 hours. The scraped Mg foil was then soaked in the solution for 24 hours.

Preparation of Mg foil with other layers. 0.876 g $Mg(TFSI)_2$ was added to 5 ml TEGDME and stirred until complete dissolution, then 0.133 g $AlCl_3$ was slowly added followed by stirring for 24 hours. The scraped Mg foil was then soaked in the solution for 24 hours.

0.861 g LiTFSI was added to 5 ml TEGDME and stirred until complete dissolution, then 0.143 g $MgCl_2$ was slowly added followed by stirring for 24 hours. The scraped Mg foil was then soaked in the solution for 24 hours.

Synthesis of electrolytes. The $Mg(TFSI)_2$/DME electrolyte was prepared by adding 0.584 g $Mg(TFSI)_2$ into 2 ml DME followed by stirring at room temperature for 24 hours. The $Mg(ClO_4)_2$/DME electrolyte and $Mg(TFSI)_2$/PC electrolyte were prepared using a similar procedure but replacing $Mg(TFSI)_2$ with $Mg(ClO_4)_2$ or DME with PC. The concentration of all three electrolytes is 0.5 M.

Electrochemical testing. All electrochemical tests were performed using 2025-type coin-cells. The

soaked Mg foils were washed in DME to remove residual solution before being used in cells. Galvanostatic cycling experiments were performed using a Neware, BST-5 V5 mA battery test system. Electrochemical impedance spectra over a frequency range from 10 kHz to either 10 or 100 mHz were obtained using an electrochemical workstation PARSTAT 2273. All of the measurements were carried out at room temperature.

Materials characterization. FTIR spectra were obtained using a Nicolet iS10 instrument. UV-vis absorption spectra were collected using a Perkin Elmer LAMBDA 1050 spectrophotometer, with the solution diluted three times before measurement. All the soaked Mg foils were thoroughly rinsed with DME or TEGDME before SEM, XPS and NEXAFS measurements. SEM and Energy-dispersive X-ray spectroscopy (EDS) images were acquired with a Zeiss ultra plus microscope, with samples transported in a sealed container from the glovebox to instrument but with a 2-3 min air exposure during loading into the SEM. XPS measurements were performed using a Thermo Nexsa system with monochromatized Al Kα X-rays. The samples were prepared in the glovebox and placed in a transfer vessel with a one-way valve. The transfer vessel was evacuated in the pre-chamber of the glove box and transferred to the XPS analysis chamber without air exposure. Adventitious carbon, C-C (284.8 eV) is used as the energy reference for all spectra. Peak fitting was performed using CASA XPS software, with a Shirley background, and applying LA (0.95,1.05,10) line shape for metallic Mg species, or LA (1.53, 243) line-shape for non-metallic species. The asymmetry index for metallic Mg is 0.062. NEXAFS spectroscopy measurements were performed in total electron yield mode (TEY) using a SR570 low-noise current amplifier (Stanford Research Systems) at beamline B07-C of the Diamond Light Source (DLS), United Kingdom. All samples were mounted on the same sample holder in the glovebox which was then heat-sealed in an aluminium laminated pouch and transferred to the beamline. The pouch was opened in a glovebag connected to the sample loadlock following three cycles of purging with Ar, and the sample immediately placed in the loadlock which was then evacuated. The beamline exit slits were opened to 800 μm in the non-dispersive direction, and 50 μm in the dispersive direction, which results in a spot size of approximately 100 × 200 μm. Spectra are normalized to the incident photon flux measured using an Au foil cleaned by repeated sputter-annealing cycles, with transient changes (e.g. electron top-up) accounted for by measurement of the photocurrent of an upstream beamline slit. Energy calibration is performed by setting the first inflection point in the derivative spectrum of the Mg K-edge of metallic Mg to 1303.0 eV[24].

Results and discussion

Mg foil with an artificial SEI (a-SEI) was prepared by soaking bare Mg foil in $AlCl_3$+LiTFSI/TEGDME for 24 hours, following the protocol described in the Methods section. FTIR spectra of the relevant solutions were acquired to reveal interactions between components within the solution and reactions with the Mg foil (see Figure 1a, where all spectra have the TEGDME solvent background subtracted). There are no obvious changes between the LiTFSI/TEGDME and $AlCl_3$+LiTFSI/TEGDME solution in the range of 700-1500 cm^{-1}, consistent with previous literature reports comparing FTIR spectra of $Al(TFSI)_3$/acetonitrile (AN) and LiTFSI/AN.[25] Strong peaks corresponding to SO_2-N-SO_2 (1060 cm^{-1}), SO_2 (1194 and 1355 cm^{-1}) and S-N (at 738 cm^{-1}) stretches are clearly present for the $AlCl_3$+LiTFSI/TEGDME solution (Figure 1a iii),[26] confirming the presence of the $TFSI^-$ anion as for the LiTFSI/TEGDME solution (Figure 1a ii). In the 600-700 cm^{-1} region, a new absorbance signal is observed at 624 cm^{-1} in the $AlCl_3$+LiTFSI/TEGDME solution, which is not present in the $AlCl_3$/TEGDME (Figure 1a i) or LiTFSI/TEGDME solutions, consistent with it arising

from interaction between the LiTFSI and $AlCl_3$. The FTIR spectra of the $AlCl_3$+LiTFSI/TEGDME solution after reacting with Mg for 24 hours exhibits another new peak at 648 cm^{-1}, and the color of the solution gradually becomes lighter as the reaction proceeds (Figure S1). This implies that the reaction between the solution and Mg foil proceeds over the course of many hours. The UV-vis absorption spectra in Figure 1b show absorption maxima whose intensities decrease as the reaction progresses, further confirming this view.

SEM and EDS were used to observe the surface morphology and composition of the Mg foil before (Figure 1c and Figure S2) and after (Figure 1d and Figure S3) soaking in the $AlCl_3$+LiTFSI/TEGDME solution for 24 h. The micrographs show no evidence of residual electrolyte salt crystals attached to the Mg surface after soaking, but a surface layer is observed that appears reasonably uniform, conformal and crack-free, even over the striations induced during cleaning of the Mg foil by scraping. A number of small pits are visible, suggesting the surface layer is somewhat porous. The Mg foil was fractured to enable observation of its cross-sectional profile (Figure 1e). EDS elemental mapping (Figure 1e overlay and Figure S4) of the section shows that the F, Cl and S Kα signals are stronger close to the surface layer compared to the Mg metal below, consistent with formation of a surface layer incorporating species from the solution used for soaking. Having confirmed the formation of a surface layer following the 24 hr soaking period, we now consider its ability to conduct Mg^{2+} and its stability during repeated stripping/plating.

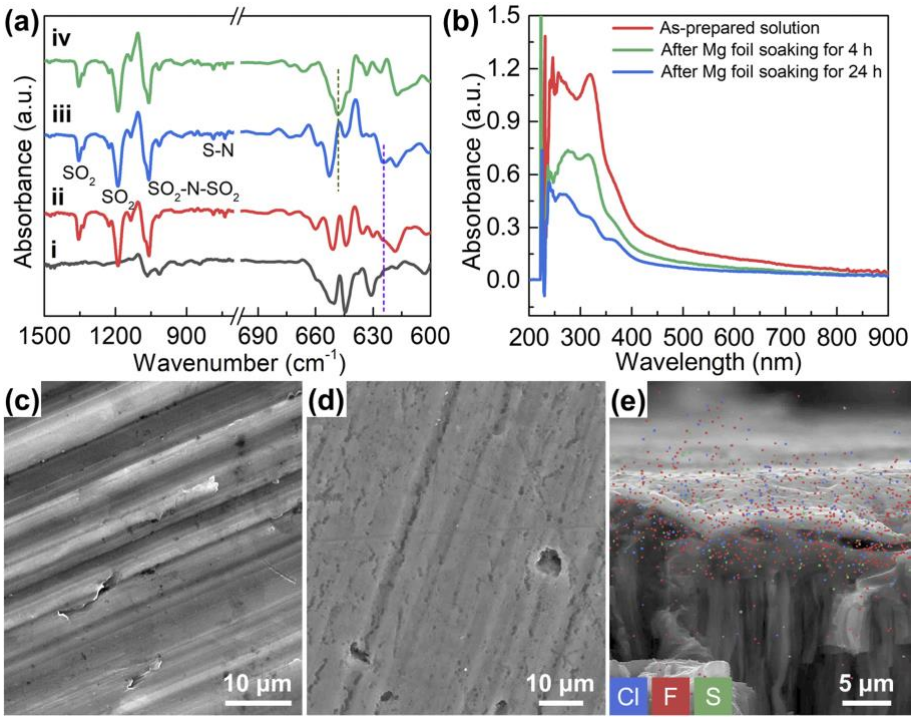

Figure 1 (a) FTIR spectra of (i) $AlCl_3$/TEGDME solution, (ii) LiTFSI/TEGDME solution as well as the $AlCl_3$+LiTFSI/TEGDME solution (iii) before and (iv) after Mg foil soaking for 24 hours. (b) UV–Vis absorption spectra of $AlCl_3$+LiTFSI/TEGDME after different Mg foil soaking times. SEM images showing plan views of (c) bare Mg foil, and (d) Mg foil soaked in $AlCl_3$+LiTFSI/TEGDME for 24 hours, and (e) a cross-section and EDS mapping of Mg foil soaked in $AlCl_3$+LiTFSI/TEGDME for 24 hours. All SEM images are acquired by secondary electron detection using an Everhart-Thornely detector.

The general applicability of the a-SEI film is explored using three different electrolyte formulations where both salt and solvent are varied: $Mg(TFSI)_2$/DME, $Mg(ClO_4)_2$/DME, and $Mg(TFSI)_2$/PC. $Mg(TFSI)_2$/DME is considered a promising MIB electrolyte with recent studies confirming Mg stripping and deposition in ethereal $Mg(TFSI)_2$ solutions albeit with large overpotentials needed to initiate stripping.[16] $Mg(ClO_4)_2$/DME exhibits lower reduction stability with ClO_4^- tending to react with Mg to form a poorly or non-conducting surface layer, and thus the application of $Mg(ClO_4)_2$ in MIBs has mainly focused on solid electrolyte systems to date.[27] $Mg(TFSI)_2$/PC offers potential advantages as the carbonate ester, which has been widely explored in Li-ion battery research, is non-corrosive and highly resistant to oxidation. However, due to its reductive decomposition on the Mg surface, a semi-carbonate interphase with negligible Mg^{2+} conductivity is formed, such that reversible Mg deposition/stripping is typically not achieved.[28]

EIS and galvanostatic discharge/charge profiles were obtained using symmetric cells consisting of bare-Mg/bare-Mg or a-SEI-Mg/a-SEI-Mg electrodes, for each of the electrolytes. Figure 2 shows Nyquist plots for these cells, fitted with the equivalent circuits shown inset. The R-C pair of the bare-Mg/bare-Mg cell corresponds to the charge transfer process, and the two R-C pairs of the a-SEI-Mg/a-SEI-Mg correspond to the migration of Mg ions in the SEI layer at relatively higher frequency and the charge transfer process at relatively lower frequency. The fitted data is summarized in Table S1. The initial impedance spectra of bare-Mg/bare-Mg for all three electrolytes exhibit depressed semicircular capacitive loops corresponding to interfacial impedances from hundreds to thousands of $k\Omega \cdot cm^{-2}$. These high interfacial impedances are attributable to the formation of a passivation layer by electrolyte decomposition on the bare Mg, that exhibits poor Mg-ion transport properties. The impedance spectra of a-SEI-Mg/a-SEI-Mg cells exhibit dramatically smaller charge transfer resistances, two orders of magnitude lower than the corresponding bare-Mg/bare-Mg cells, indicating the a-SEI formed is more ionically conductive and comparatively faster charge transfer occurs at the Mg metal interface. EIS measurements for shorter soaking times in $AlCl_3$+LiTFSI/TEGDME (4 hrs, 10hrs, Figure S5) reveal that R_{SEI} and R_{ct} decrease gradually with increasing soaking time, further indicating a-SEI formation proceeds over a number of hours.

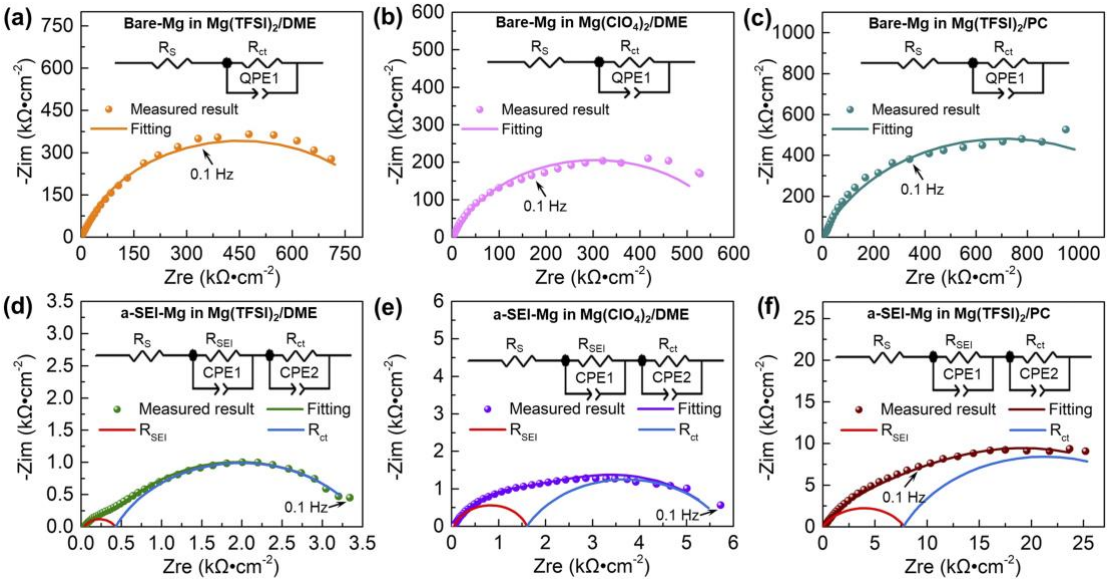

Figure 2 EIS spectra of bare-Mg/bare-Mg and a-SEI-Mg/a-SEI-Mg cells: (a) bare-Mg in $Mg(TFSI)_2$/DME, (b) bare-Mg in $Mg(ClO_4)_2$/DME, (c) bare-Mg in $Mg(TFSI)_2$/PC, (d) a-SEI-Mg in

$Mg(TFSI)_2$/DME, (e) a-SEI-Mg in $Mg(ClO_4)_2$/DME and (f) a-SEI-Mg in $Mg(TFSI)_2$/PC electrolytes . (d) The insets show the equivalent circuits used for fitting.

For each electrode-electrolyte combination, repeated galvanostatic charge/discharge cycles were performed at half-hour intervals at a current density of 0.01 mA/cm^2 (switching to potentiostatic cycling if the voltage exceeded the range of -3 V to 5 V). As shown in Figure 3, the bare-Mg/bare-Mg cells display relatively large overpotentials of the order of volts in all three electrolytes, and soon fail to deposit and strip at the desired current density in the $Mg(ClO_4)_2$/DME and $Mg(TFSI)_2$/PC electrolytes after only a few cycles. In the $Mg(TFSI)_2$/DME electrolyte, the overpotential grows during the first 8 cycles but then becomes reasonably stable at a lower value of around 2.4 V (Figure 3a). This is attributable to an initial period during which a stable layer forms by electrolyte decomposition that does not completely passivate the surface, thereby allowing Mg deposition and stripping to proceed, however the relatively large overpotential indicates rather poor Mg^{2+} conductivity for this layer. For the $Mg(ClO_4)_2$/DME and $Mg(TFSI)_2$/PC electrolytes which are known to be more vulnerable to reduction, the overpotential of the bare-Mg/bare-Mg cells is seen to increase every cycle, ultimately exceeding the voltage limits of -3V to 5V used herein (Figure 3b and 3d). This behavior implies the ongoing reduction of the electrolytes on the Mg surface during charge and discharge which eventually completely passivates their surface. This is consistent with prior understanding of bare Mg electrodes in electrolytes containing ClO_4^- and PC where non-conductive interphases are expected to form by the reductive decomposition of these electrolytes[28]. Electrochemical impedance spectroscopy was further performed to elaborate this phenomenon (Figure S 6). By comparing the impedance between the cells before and after 20 cycles, it can be seen that there is a substantial reduction of the interfacial resistance in the cell with $Mg(TFSI)_2$/DME electrolyte indicating a more Mg^{2+} permeable layer forms with cycling. However, the cells with $Mg(ClO_4)_2$/DME and $Mg(TFSI)_2$/PC electrolytes do not exhibit such a lowering of impedance after continued cycling, but rather a gradual increase. This impedance increase is attributable to the growth of an ion-blocking layer that forms either as a result of the ~20 hours of contact between the Mg electrodes and electrolyte and/or ongoing electrochemical decomposition of electrolyte on the electrode surface. Furthermore, SEM pictures in Figure S 7 show an abundance of dissolution pits on the Mg electrode in $Mg(TFSI)_2$/DME electrolyte, attributable to localized Mg stripping that may be related to thinner, or higher conductivity regions in the ion-blocking layer. No such indication of Mg stripping is found for the $Mg(ClO_4)_2$/DME and $Mg(TFSI)_2$/PC electrolytes. Combined with the results of galvanostatic discharge/charge and electrochemical impedance, this suggests that no significant deposition or stripping of Mg is realized in the bare-Mg/bare-Mg cells with $Mg(ClO_4)_2$/DME and $Mg(TFSI)_2$/PC, and instead electrolyte decomposition increasingly passivates the electrode surfaces.

Symmetric cells made using the Mg electrodes with a-SEI are found to exhibit low overpotentials and reasonable deposition/stripping performance in all three electrolytes at current densities of 0.01 mA cm^{-1}. In $Mg(TFSI)_2$/DME electrolyte, the overpotential is reduced by 2 V compared to the bare Mg electrode (Figure 3a), and although it grows slightly from ~0.2 V to ~0.3 V in the first 5 half-cycles it remains extremely stable at ~0.3 V across subsequent cycles (the voltage response for 1000 h of cycling is shown in Figure S8). This stable and low overpotential indicates that with the a-SEI present reversible Mg deposition and stripping is achieved. SEM imaging shows that the morphology of the a-SEI-Mg after one half-cycle of Mg deposition (Figure S9a), an additional half-cycle of stripping (Figure S9b), and after 20 full cycles (Figure S10 a) remains similar to before cycling (Figure S3a). There is no significant additional pit formation, which would otherwise indicate localized Mg deposition/stripping. Together with the cycling data, this suggests that the a-SEI remains intact and relatively homogeneous

during cycling, and is effective in preventing the Mg from direct chemical reaction with $TFSI^-$ while still allowing the passage of Mg-ions for plating and stripping. EIS of the symmetric a-SEI-Mg/a-SEI-Mg cell after 20 half-cycles, indicates R_{SEI} and R_{ct} are less distinct but have not dramatically increased, and a straight line is apparent in the low frequency region (Figure S11), consistent with the involvement of diffusion processes. The polarization is found to remain low even at a higher current density of 0.1 mA cm^{-1} (Figure S12), where it stays below 0.35 V during 300 h of cycling.

For a-SEI-Mg/a-SEI-Mg in a $Mg(ClO_4)_2$/DME electrolyte, the polarization is around 0.5 V for the first six cycles, then suddenly drops to 0.2 V, and then slowly increases back to 0.6 V after ten cycles or so. The presence of the a-SEI therefore again leads to a relatively stable and low overpotential potential, in sharp contrast to when bare Mg electrodes are used (Figure 3c). However, we note that the overpotential is not quite as stable or as low as in $Mg(TFSI)_2$/DME indicating that the a-SEI may evolve somewhat during continued cycling. This may relate to differences in the adsorbed ions at the anode surface for these two electrolytes. Indeed the different adsorption and desolvation energies of species at the electrode surface may lead to different Mg deposition/stripping overpotentials, which may in turn induce changes in the a-SEI layer. Comparison of SEM images before and after cycling (Figure S10 b) again indicates little change in the surface morphology consistent with the a-SEI layer remaining reasonably stable and homogeneous in the $Mg(ClO_4)_2$/DME electrolyte.

Significantly, the behavior of the Mg electrodes with a-SEI in $Mg(TFSI)_2$/PC electrolyte is found to be quite different. Whilst the magnitude of the overpotential remains relatively low and constant (~0.2 V) over the first ~15 cycles (Figure 3e), indicating effective Mg deposition/stripping, the polarization is subsequently seen to increase with cycle number and the cycling curve loses its quasi-rectangular character, presumably due to degradation of the a-SEI layer in the PC solvent. Nevertheless, the overpotential after 25 cycles remains below that seen initially for the bare Mg electrodes in the same solvent. Unfortunately, the cell with $Mg(TFSI)_2$/PC electrolyte eventually fails at the 30^{th} cycle, and the SEM shows that the morphology of the Mg electrode after cycling (Figure S10 c) is also quite different. Abundant magnesium dissolution pits appear on the surface indicating localized stripping of Mg which may correlate with damaged regions of the a-SEI, suggesting that the a-SEI gradually loses its protective effect. This different behaviour compared to $Mg(TFSI)_2$/DME can be rationalized by considering the significant impact solvent choice can have on the stability the a-SEI, as well as on the viscosity and ionic conductivity of an electrolyte, leading to different ion distributions and overpotentials during Mg deposition/stripping.[29] Furthermore, changes in the strength of bonding between TFSI- ions, Mg-ions, and solvent molecules can affect electrolyte decomposition and the deposition of Mg metal.[30] We therefore suggest that the a-SEI either partly dissolves or its composition is changed through reaction with decomposition products of the $Mg(TFSI)_2$/PC electrolyte, such that its ability to conduct Mg ions is reduced, and a greater deposition and stripping overpotential is thus required. The localized stripping of Mg observed is likely the result of inhomogenous Mg-ion conductivity in the resulting passivation layer.

In order to explore the importance of $AlCl_3$ and LiTFSI during the a-SEI formation process, repeated galvanostatic charge/discharge cycles where performed for symmetric cells made with Mg foils soaked either in $MgCl_2$+LiTFSI/TEGDME or $AlCl_3$+$Mg(TFSI)_2$/TEGDME solution. The polarization of these cells is found to initially be intermediate between the a-SEI-Mg and bare-Mg symmetric cells. However, the polarization fluctuates greatly with cycling, and short circuits occur after around ten cycles (Figure S14 and S15) confirming that soaking in these solutions does not yield a similar a-SEI. This suggests that the conformational states of $TFSI^-$ in the three solutions are different,

presumably due to the different cation sizes and ionic strengths of the Al^{3+}, Mg^{2+}, and Li^{+}.[31] The decomposition products of $TFSI^-$ on Mg in the $AlCl_3$+LiTFSI/TEGDME solution appear to facilitate effective Mg-ion transfer whilst preventing passivation in the 3 electrolytes considered. The films formed by soaking in $MgCl_2$+LiTFSI/TEGDME and $AlCl_3$+$Mg(TFSI)_2$/TEGDME behave differently to the bare-Mg in $Mg(TFSI)_2$/DME electrolyte, partially protecting the Mg from the passivation of the electrolyte, but as cycling progresses, stable Mg ion stripping/plating cannot be achieved.

In summary, the a-SEI layer shows the ability to conduct Mg-ions, as indicated by reversible deposition/stripping behavior and significantly reduced impedance compared to bare Mg electrodes. Mg electrodes protected with a-SEI exhibit excellent reversibility for 100 h in $Mg(TFSI)_2$/DME and $Mg(ClO_4)_2$/DME electrolytes without pronounced overpotential build-up during extended cycling, and the a-SEI also enables reversible electrochemical cycling even in the PC based electrolyte.

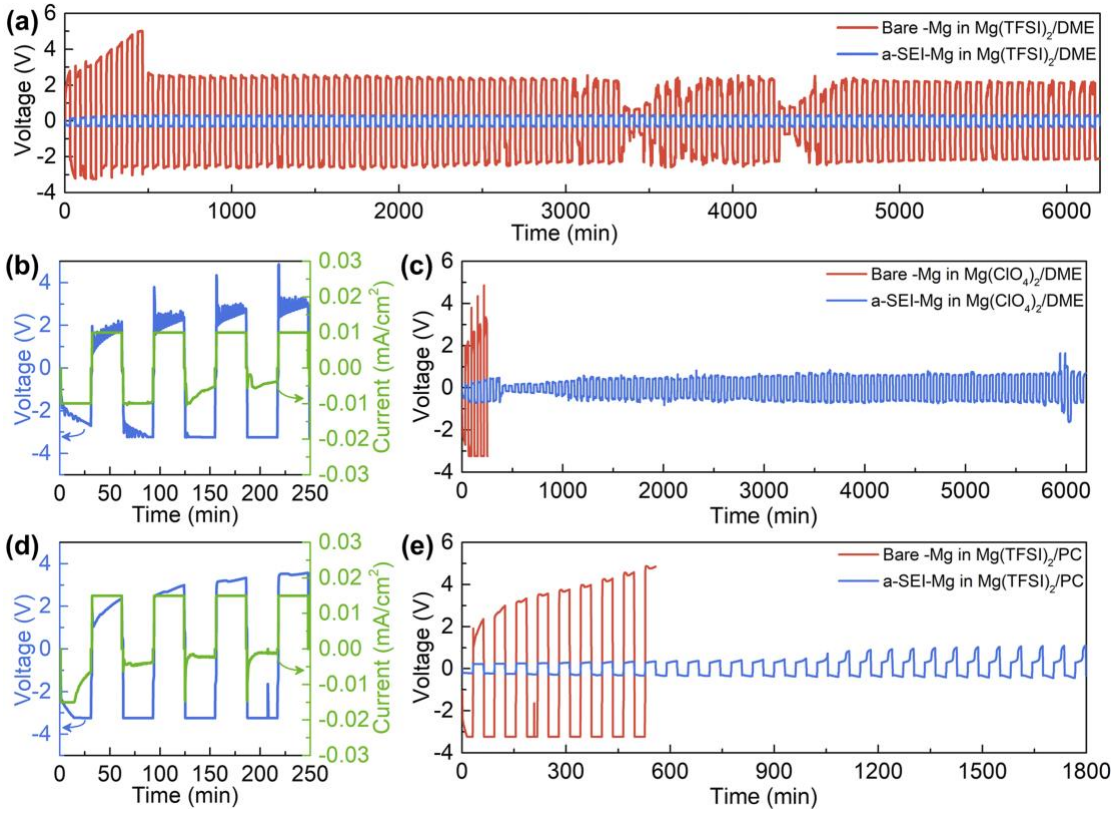

Figure 3 Voltage responses of bare-Mg/bare-Mg and a-SEI-Mg/a-SEI-Mg cells in different electrolyte systems at current density of 0.01 mA cm^{-1}. (a) $Mg(TFSI)_2$/DME electrolyte, (b-c) $Mg(ClO_4)_2$/DME electrolyte, (d-e) $Mg(TFSI)_2$/PC electrolytes. Where b and d are the first four cycles of the cells with bare Mg electrodes in c and e. In some cases, the voltage exceeded the range of -3 V to 5 V, and the cells were switched to potentiostatic cycling.

To better understand the chemical structure of the surface layers that form on the Mg, XPS measurements were performed on freshly prepared bare Mg, the a-SEI, and the passivation layer formed by soaking in $Mg(TFSI)_2$/TEGDME solution. All were directly transferred from the glovebox to the XPS sample chamber using a vacuum transfer vessel avoiding ambient exposure. A survey scan of LiTFSI+$AlCl_3$/TEGDME immersed Mg foil shows the presence of Mg, F, Cl, S, O, and C species on the surface while N, Al and Li species are not detected (Figures S16, S17), suggesting that not only

$TFSI^-$ ions but also Cl^- ions are involved in formation of the a-SEI layer. Considering the Mg 2p core level spectra, the binding energies of MgO, $Mg(OH)_2$, MgF_2, and MgS lie close to each other at ~50.8 eV,[32-35] whilst $MgCl_2$ and $MgCO_3$ both lie close to ~51.9 eV,[34, 36] making direct analysis potentially ambiguous. We therefore first consider the core levels of the other elements. The absence of any detectable signal in the N 1s region (Figure S17) confirms that the sample rinsing procedure is effective in removing electrolyte residue related to $TFSI^-$. The Cl 2p XPS spectrum in Figure 4a confirms the existence of $MgCl_2$ and organic compounds containing C-Cl bonds,[37] with the amount of Cl in $MgCl_2$ approximately three times that in organic compounds based on the peak areas. The F 1s XPS spectrum (Figure 4b) indicates the presence of two main F-containing species on the surface at binding energies of 684.8 eV and 688.2 eV, assigned to MgF_2 and $-CF_3$ respectively.[38] Since no significant $TFSI^-$ contribution is expected based on the N1s region, the MgF_2 and $-CF_3$ are attributable to products of $TFSI^-$ reduction on the Mg surface during a-SEI layer formation. Similarly, the S 2p spectrum (Figure 4c) is fitted with species attributable to inorganic MgS (S $2p_{3/2}$ located at 161.2 eV, ΔE = 1.16 eV) and organic peaks representing $-C-SO_X-C-$ (X=2,3) (169.2 eV, 166.7 eV) and C-S (164.5 eV) respectively [39, 40]. The components identified correspond well with the features in the Mg 2p and C 1s spectra, within the limits of overlapping peaks discussed earlier. The significant peaks of $-CF_3$ (located at 293.0 eV), C=O (288.0 eV), C-Cl (287.0 eV), C-O/C-S (286.4 eV) and C-C (284.8 eV) in the C 1s spectrum (Figure S18) confirm the presence of various carbonaceous components.[38, 41-43] Considering the Mg-containing components in the above spectra, the spectrum of Mg 2p (Figure 4d) can be assigned to three main species, corresponding to Mg^0 at 49.6 eV, MgF_2/MgS at 51.0 eV and $MgCl_2$ at 51.7 eV respectively. The XPS results in Figure 4(a-d) lead to the conclusion that the surface of the a-SEI layer is composed of inorganic components such as MgF_2, $MgCl_2$, MgS and possibly some minor MgO and $Mg(OH)_2$ contributions as well as organic components, but largely free of intact $TFSI^-$.

In contrast to the a-SEI layer, XPS measurements of the passivation layer, formed by immersion of Mg foil in $Mg(TFSI)_2$/TEGDME solution for 24 hours, show not only F, S, Mg, C, and O species but also a small N 1s contribution on the surface apparent in the survey spectrum (Figure S19). The N 1s core level spectrum in Figure 4e shows a single peak at ~400.0 eV attributable to $TFSI^-$.[38, 44] Further evidence for the presence of $TFSI^-$ comes from the F 1s spectra (Figure 4f) where two species corresponding to $-CF_3$ and -CF can be observed, with the dominance of the former species consistent with $TFSI^-$ incorporated into the passivation layer or adsorbed on its surface. In addition, the spectrum of S 2p in Figure 4g exhibits only a single pair of peaks which are assigned to $TFSI^-$,[44] and lacks the MgS component seen in the a-SEI. The Mg 2p core level spectrum in Figure 4h shows that some of the inorganic components seen in the a-SEI such as MgF_2, $MgCl_2$ and MgS are absent from the passivation layer, whilst MgO/$Mg(OH)_2$ and $MgCO_3$ are now observed (see also C 1s spectrum – Figure S20).[33, 45] Furthermore the Mg^0 component is significantly weaker than for the a-SEI, suggesting that the passivation layer is appreciably thicker than the a-SEI.

According to these observations, the a-SEI layer is distinguished by its content of MgF_2, MgS and $MgCl_2$, whereas the much thicker passivation layer formed in $Mg(TFSI)_2$/TEGDME is rich in $MgCO_3$ as well as MgO/$Mg(OH)_2$, and incorporates intact $TFSI^-$. Although bulk MgF_2, $MgCl_2$, and MgS have high diffusion barriers for Mg ion transport,[49, 50] their presence as SEI components has previously been reported.[46-48] Given the nanometer scale thickness of the a-SEI (<10 nm, given Mg^0 is readily resolved in XPS) and the combination of organic and inorganic constituents, abundant grain boundaries and local variations in chemical composition may facilitate the Mg-ion transport observed herein.

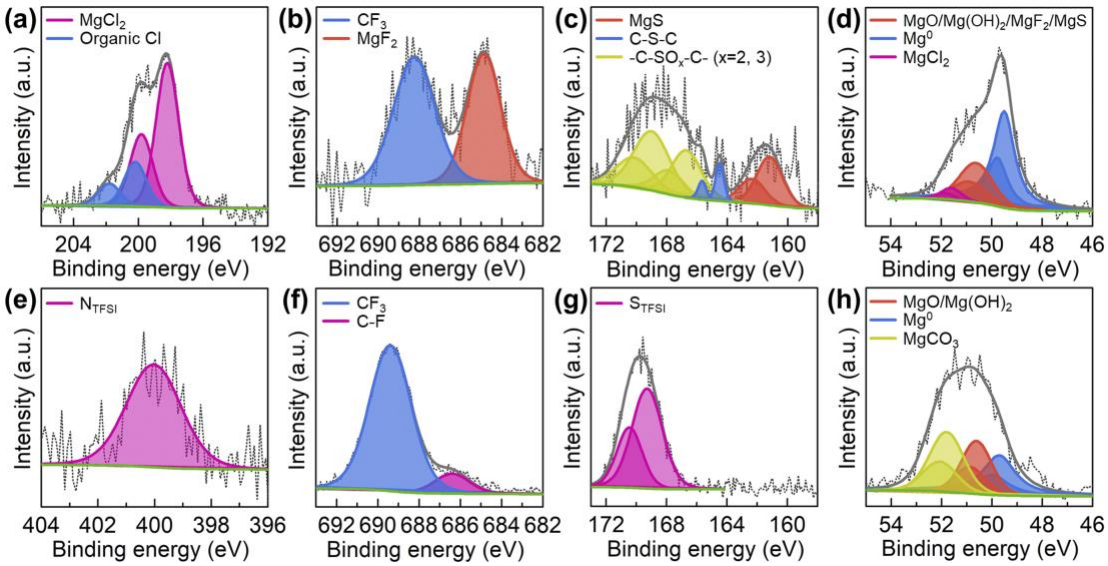

Figure 4. High resolution XP spectra of the a-SEI Mg interface (a-d) and the passivation layer formed on Mg in $Mg(TFSI)_2$/TEGDME (e-h) covering the Cl 2p (a), F 1 s (b, f), S 2p (c,g), Mg 2p (d,h) and N 1s (e) core levels.

Synchrotron-based NEXAFS measurements were also performed in total electron yield (TEY) mode (~10 nm information depth) to further investigate the surface chemistry of these samples. Figure 5 shows the Mg, O, and C K-edge absorption spectra of the bare Mg, a-SEI Mg and passivated Mg. All spectra have been processed by subtraction of a linear background fitted to the pre-edge region and normalization of the post-edge. The NEXAFS spectra have contributions from multiple species whose features can be complex and overlap. Based on reference spectra from literature, the Mg K-edges are assigned using the following key features for candidate species: Mg^0 with the first near edge feature at ~1305 eV, MgO with main features at ~1309, ~1315, and ~1317 eV, $Mg(OH)_2$ with main feature at ~1314 eV and an additional small feature at ~1328 eV, $MgCO_3$ with main features at 1311 and 1313 eV, $MgCl_2$/MgS both with main feature at ~1310 eV, and MgF_2 with main feature at 1315 eV.[24, 51-54]

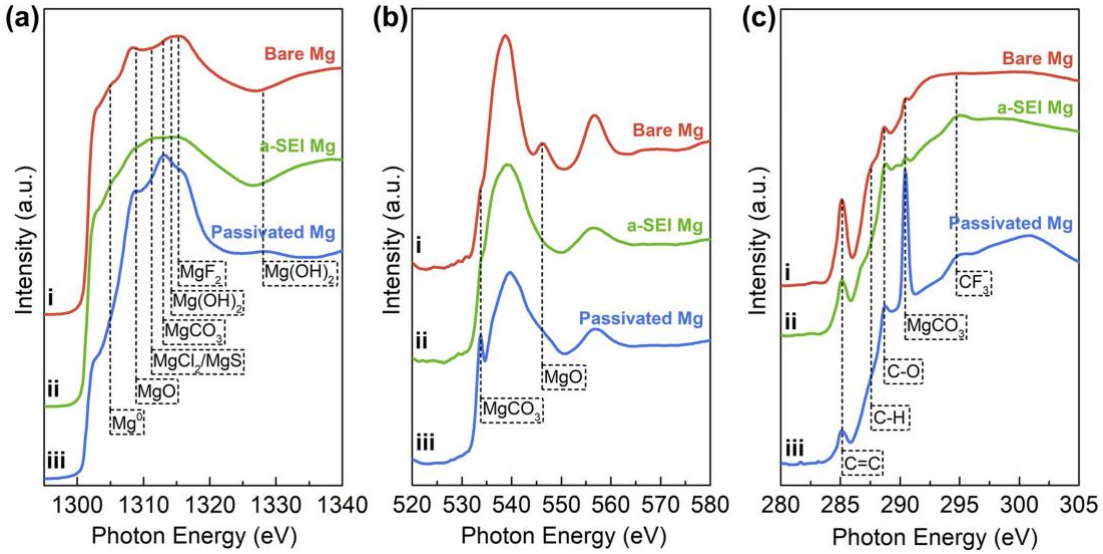

Figure 5 (a) C K-edge, (b) O K-edge and (c) Mg K-edge NEXAFS spectra of different Mg foils. Where the i, ii and iii are bare Mg, a-SEI Mg and passivated Mg respectively.

As seen in Figure 5a (i), the bare Mg resembles metallic Mg with some MgO coverage,[54] as well as small $Mg(OH)_2$ and $MgCO_3$ contributions indicating surface reaction with residual contaminants from the glovebox environment and during transfer to the beamline. The O K-edge and C K-edge (Figure 5b,c i) further confirm the presence of MgO at the surface, with the feature at 546.0 eV distinguishing from other candidate species,[52, 55] whilst small contributions at 533.7 eV and 290.4 eV are consistent with $MgCO_3$.[56] Note the C K-edge features at 285.1 eV, 287.5, and 288.6 eV are seen for all samples and are attributable to 1s → π* transitions of C=C, C-H, and C-O bonds typical of adventitious carbon.[57]

The Mg K-edge spectrum of the a-SEI Mg (Figure 5a ii) shows a similarly strong metallic Mg contribution, but with considerably decreased MgO features and the emergence of $MgCl_2$/MgS features and possibly MgF_2. This is consistent with the a-SEI having a similar thickness to the thin layer formed on the bare Mg due to residual contaminants, although its chemistry is clearly different. The O K-edge Figure 5 (b ii) shows suppression of the feature at 546.0 eV again confirming the lower MgO content, whilst the intensities of the $MgCO_3$ feature at 533.7 eV and the corresponding feature at 290.4 eV in the C K-edge (Figure 5 c ii) show little variation, indicating the $MgCO_3$ content is relatively unchanged. The C K-edge also shows an additional feature at 294.7 eV assigned to CF_3 related to $TFSI^-$ decomposition,[58] consistent with the XPS results.

In sharp contrast, the Mg K-edge spectrum of Mg foil passivated by soaking in $Mg(TFSI)_2$/TEGDME solution (Figure 5a iii) shows a much weaker metallic component and more pronounced MgO, and $Mg(OH)_2$ features indicating the passivation layer formed over the metallic Mg is much thicker than the a-SEI. $MgCO_3$ is also present but harder to distinguish due to overlap with the features of these other species. However, the O and C K-edges in Figure 5 (b-c iii) reveal intense $MgCO_3$ features which are much stronger than for the bare Mg foil (sample i). Furthermore, the O K-edge shows a weak feature at 546.0 eV attributable to the presence of some MgO, and the CF_3 feature is again present in the C K-edge consistent with the XPS results. Together this indicates significant $MgCO_3$ and $Mg(OH)_2$ content in the passivation layer that is attributable to $Mg(TFSI)_2$ decomposition, whereas the MgO may persist from the freshly prepared Mg.

The NEXAFS analysis therefore further demonstrates that $MgCl_2$ and MgS are present in the a-SEI layer whilst MgO is suppressed which may contribute to its low overpotential for Mg plating/stripping and cycling stability. On the other hand, the passivation layer formed in $Mg(TFSI)_2$/TEGDME solution is much thicker than the a-SEI and contains $MgCO_3$, $Mg(OH)_2$, and MgO as significant components. An overview of the components present in the a-SEI and passivation layer is provided in Table 1.

Table 1 Components present in the a-SEI and surface passivation layer

	Inorganic		Organic			
	$MgCl_2$, MgF_2, MgS	MgO, $Mg(OH)_2$, $MgCO_3$	C-Cl, C-S, SO_x(x=2, 3)	CF_3	CF	$TFSI^-$
a-SEI layer	✓	Limited	✓	✓	-	-
Passivation layer	-	Abundant	-	✓	✓	✓

Conclusions

In summary, this study presents a new approach to overcoming the incompatibility of metallic Mg anodes with several organic electrolytes. An a-SEI layer synthesized by soaking Mg foil in

LiTFSI+$AlCl_3$/TEGDME solution is found to exhibit promising Mg^{2+} conductivity, leading to relatively low and stable overpotentials during repeated stripping and plating of Mg, as well as avoiding complete passivation of the Mg surface even in electrolytes with poor reduction stability. The structure and composition of the a-SEI layer and the passivation layer formed when it is not present are revealed through surface sensitive X-ray spectroscopies. XPS and NEXAFS analyses reveal differences in thickness and chemical structure between the a-SEI and passivation layer: (1) The a-SEI is found to be significantly thinner than the passivation layer. (2) The a-SEI has more abundant MgF_2, $MgCl_2$ and MgS species, while the passivation layer has larger contributions from $MgCO_3$, $Mg(OH)_2$ and MgO. (3) Intact $TFSI^-$ is adsorbed onto or incorporated into the passivation layer which isn't seen for the a-SEI. We therefore suggest that the presence of the MgF_2, $MgCl_2$ and MgS species are beneficial in realizing a stable a-SEI layer that effectively transports Mg ions, whilst the formation of $MgCO_3$ and $Mg(OH)_2$ by decomposition of $TFSI^-$ and the persistence of MgO result in undesirable passivation of the Mg anode.

Acknowledgement
This research was supported by the National Natural Science Foundation of China (no. 51772068), and the Faraday Institution (faraday.ac.uk; grant numbers FIRG011). We acknowledge Diamond Light Source for time on Beamline B07C under proposal SI21925-1. Y.L. is grateful to DLS and the Research Complex at Harwell for hosting her during an extended research visit.

Supporting Information
Optical images of $AlCl_3$+LiTFSI/TEG solution after different Mg soaking time; Additional EIS spectra and Electrochemical Cell Testing Data; SEM images, EDS and XPS spectra of Mg electrodes.

References
1. Muldoon, J.; Bucur, C. B.; Gregory, T., Quest for nonaqueous multivalent secondary batteries: magnesium and beyond. *Chemical reviews* **2014,** *114* (23), 11683-720.
2. Saha, P.; Datta, M. K.; Velikokhatnyi, O. I.; Manivannan, A.; Alman, D.; Kumta, P. N., Rechargeable magnesium battery: Current status and key challenges for the future. *Progress in Materials Science* **2014,** *66*, 1-86.
3. Zhang, Y.; Geng, H.; Wei, W.; Ma, J.; Chen, L.; Li, C. C., Challenges and recent progress in the design of advanced electrode materials for rechargeable Mg batteries. *Energy Storage Materials* **2019,** *20*, 118-138.
4. Jäckle, M.; Helmbrecht, K.; Smits, M.; Stottmeister, D.; Groß, A., Self-diffusion barriers: possible descriptors for dendrite growth in batteries? *Energy & Environmental Science* **2018,** *11* (12), 3400-3407.
5. Aurbach, D.; Lu, Z.; Schechter, A.; Gofer, Y.; Gizbar, H.; Turgeman, R.; Cohen, Y.; Moshkovich, M.; Levi, E., Prototype systems for rechargeable magnesium batteries. *Nature* **2000,** *407* (6805), 724-7.
6. Gregory, T. D.; Hoffman, R. J.; Winterton, R. C., Nonaqueous Electrochemistry of Magnesium - Applications to Energy-Storage. *Journal of the Electrochemical Society* **1990,** *137* (3), 775-780.
7. Aurbach, D.; Suresh, G. S.; Levi, E.; Mitelman, A.; Mizrahi, O.; Chusid, O.; Brunelli, M., Progress in Rechargeable Magnesium Battery Technology. *Advanced materials* **2007,** *19* (23), 4260-4267.

8. Kim, H. S.; Arthur, T. S.; Allred, G. D.; Zajicek, J.; Newman, J. G.; Rodnyansky, A. E.; Oliver, A. G.; Boggess, W. C.; Muldoon, J., Structure and compatibility of a magnesium electrolyte with a sulphur cathode. *Nature communications* **2011,** *2*, 427.
9. Zhao-Karger, Z.; Zhao, X.; Wang, D.; Diemant, T.; Behm, R. J.; Fichtner, M., Performance Improvement of Magnesium Sulfur Batteries with Modified Non-Nucleophilic Electrolytes. *Advanced Energy Materials* **2015,** *5* (3), 1401155.
10. Benmayza, A.; Ramanathan, M.; Arthur, T. S.; Matsui, M.; Mizuno, F.; Guo, J.; Glans, P.-A.; Prakash, J., Effect of Electrolytic Properties of a Magnesium Organohaloaluminate Electrolyte on Magnesium Deposition. *The Journal of Physical Chemistry C* **2013,** *117* (51), 26881-26888.
11. Barile, C. J.; Spatney, R.; Zavadil, K. R.; Gewirth, A. A., Investigating the Reversibility of in Situ Generated Magnesium Organohaloaluminates for Magnesium Deposition and Dissolution. *The Journal of Physical Chemistry C* **2014,** *118* (20), 10694-10699.
12. Xu, H.; Zhang, Z.; Cui, Z.; Du, A.; Lu, C.; Dong, S.; Ma, J.; Zhou, X.; Cui, G., Strong anion receptor-assisted boron-based Mg electrolyte with wide electrochemical window and non-nucleophilic characteristic. *Electrochemistry Communications* **2017,** *83*, 72-76.
13. Du, A.; Zhang, Z.; Qu, H.; Cui, Z.; Qiao, L.; Wang, L.; Chai, J.; Lu, T.; Dong, S.; Dong, T.; Xu, H.; Zhou, X.; Cui, G., An efficient organic magnesium borate-based electrolyte with non-nucleophilic characteristics for magnesium–sulfur battery. *Energy & Environmental Science* **2017,** *10* (12), 2616-2625.
14. Attias, R.; Salama, M.; Hirsch, B.; Goffer, Y.; Aurbach, D., Anode-Electrolyte Interfaces in Secondary Magnesium Batteries. *Joule* **2019,** *3* (1), 27-52.
15. Rajput, N. N.; Qu, X.; Sa, N.; Burrell, A. K.; Persson, K. A., The coupling between stability and ion pair formation in magnesium electrolytes from first-principles quantum mechanics and classical molecular dynamics. *Journal of the American Chemical Society* **2015,** *137* (9), 3411-20.
16. Ha, S. Y.; Lee, Y. W.; Woo, S. W.; Koo, B.; Kim, J. S.; Cho, J.; Lee, K. T.; Choi, N. S., Magnesium(II) bis(trifluoromethane sulfonyl) imide-based electrolytes with wide electrochemical windows for rechargeable magnesium batteries. *ACS applied materials & interfaces* **2014,** *6* (6), 4063-73.
17. Yoo, H. D.; Han, S. D.; Bolotin, I. L.; Nolis, G. M.; Bayliss, R. D.; Burrell, A. K.; Vaughey, J. T.; Cabana, J., Degradation Mechanisms of Magnesium Metal Anodes in Electrolytes Based on (CF3SO2)2N- at High Current Densities. *Langmuir : the ACS journal of surfaces and colloids* **2017**.
18. Arthur, T. S.; Glans, P.-A.; Singh, N.; Tutusaus, O.; Nie, K.; Liu, Y.-S.; Mizuno, F.; Guo, J.; Alsem, D. H.; Salmon, N. J.; Mohtadi, R., Interfacial Insight from Operando XAS/TEM for Magnesium Metal Deposition with Borohydride Electrolytes. *Chemistry of Materials* **2017,** *29* (17), 7183-7188.
19. Sakuma, M.; Suzuki, K.; Hirayama, M.; Kanno, R., Reactions at the electrode/electrolyte interface of all-solid-state lithium batteries incorporating Li–M (M = Sn, Si) alloy electrodes and sulfide-based solid electrolytes. *Solid State Ionics* **2016,** *285*, 101-105.
20. Wenzel, S.; Sedlmaier, S. J.; Dietrich, C.; Zeier, W. G.; Janek, J., Interfacial reactivity and interphase growth of argyrodite solid electrolytes at lithium metal electrodes. *Solid State Ionics* **2018,** *318*, 102-112.
21. Son, S.-B.; Gao, T.; Harvey, S. P.; Steirer, K. X.; Stokes, A.; Norman, A.; Wang, C.; Cresce, A.; Xu, K.; Ban, C., An artificial interphase enables reversible magnesium chemistry in carbonate electrolytes. *Nature Chemistry* **2018,** *10* (5), 532-539.

22. Luo, J.; Li, Y.; Zhang, H.; Wang, A.; Lo, W. S.; Dong, Q.; Wong, N.; Povinelli, C.; Shao, Y.; Chereddy, S.; Wunder, S.; Mohanty, U.; Tsung, C. K.; Wang, D., Metal-Organic Framework Thin Film for Selective Mg2+ Transport. *Angewandte Chemie* **2019**.
23. Yim, T.; Woo, S.-G.; Lim, S.-H.; Yoo, J.-Y.; Cho, W.; Park, M.-S.; Han, Y.-K.; Kim, Y.-J.; Yu, J., Magnesium Anode Pretreatment Using a Titanium Complex for Magnesium Battery. *ACS Sustainable Chemistry & Engineering* **2017,** *5* (7), 5733-5739.
24. Bearden, J. A.; Burr, A. F., Reevaluation of X-Ray Atomic Energy Levels. *Reviews of Modern Physics* **1967,** *39* (1), 125-142.
25. Chiku, M.; Matsumura, S.; Takeda, H.; Higuchi, E.; Inoue, H., Aluminum Bis(trifluoromethanesulfonyl)imide as a Chloride-Free Electrolyte for Rechargeable Aluminum Batteries. *Journal of the Electrochemical Society* **2017,** *164* (9), A1841-A1844.
26. Theivaprakasam, S.; Girard, G.; Howlett, P.; Forsyth, M.; Mitra, S.; MacFarlane, D., Passivation behaviour of aluminium current collector in ionic liquid alkyl carbonate (hybrid) electrolytes. *npj Materials Degradation* **2018,** *2* (1).
27. Ekanayake, P.; Dissanayake, M. A. K. L., Effect of nanoporous alumina filler on conductivity enhancement in PEO9(MgClO4)2 polymer electrolyte: a 1H NMR study. *Journal of Solid State Electrochemistry* **2008,** *13* (12), 1825-1829.
28. Lu, Z.; Schechter, A.; Moshkovich, M.; Aurbach, D., On the electrochemical behavior of magnesium electrodes in polar aprotic electrolyte solutions. *Journal of Electroanalytical Chemistry* **1999,** *466* (2), 203-217.
29. Hu, X. C.; Shi, Y.; Lang, S. Y.; Zhang, X.; Gu, L.; Guo, Y. G.; Wen, R.; Wan, L. J., Direct insights into the electrochemical processes at anode/electrolyte interfaces in magnesium-sulfur batteries. *Nano Energy* **2018,** *49*, 453-459.
30. Tuerxun, F.; Yamamoto, K.; Hattori, M.; Mandai, T.; Nakanishi, K.; Choudhary, A.; Tateyama, Y.; Sodeyama, K.; Nakao, A.; Uchiyama, T.; Matsui, M.; Tsuruta, K.; Tamenori, Y.; Kanamura, K.; Uchimoto, Y., Determining Factor on the Polarization Behavior of Magnesium Deposition for Magnesium Battery Anode. *ACS applied materials & interfaces* **2020,** *12* (23), 25775-25785.
31. Chen, Y.; Jaegers, N. R.; Han, K. S.; Wang, H.; Young, R. P.; Agarwal, G.; Lipton, A. S.; Assary, R. S.; Washton, N. M.; Hu, J. Z.; Mueller, K. T.; Murugesan, V., Probing Conformational Evolution and Associated Dynamics of Mg(N(SO2CF3)2)2·Dimethoxyethane Adduct Using Solid-State 19F and 1H NMR. *The Journal of Physical Chemistry C* **2020,** *124* (9), 4999-5008.
32. Mertin, S.; Marot, L.; Sandu, C. S.; Steiner, R.; Scartezzini, J.-L.; Muralt, P., Nanocrystalline Low-Refractive Magnesium Fluoride Films Deposited by Reactive Magnetron Sputtering: Optical and Structural Properties. *Advanced Engineering Materials* **2015,** *17* (11), 1652-1659.
33. Jerome, R.; Teyssie, P.; Pireaux, J. J.; Verbist, J. J., Surface-Analysis of Polymers End-Capped with Metal Carboxylates Using X-Ray Photoelectron-Spectroscopy. *Applied Surface Science* **1986,** *27* (1), 93-105.
34. Saleh, H.; Weling, T.; Seidel, J.; Schmidtchen, M.; Kawalla, R.; Mertens, F. O. R. L.; Vogt, H. P., An XPS Study of Native Oxide and Isothermal Oxidation Kinetics at 300 °C of AZ31 Twin Roll Cast Magnesium Alloy. *Oxidation of Metals* **2013,** *81* (5-6), 529-548.
35. Nakayama, Y.; Matsumoto, R.; Kumagae, K.; Mori, D.; Mizuno, Y.; Hosoi, S.; Kamiguchi, K.; Koshitani, N.; Inaba, Y.; Kudo, Y.; Kawasaki, H.; Miller, E. C.; Weker, J. N.;

Toney, M. F., Zinc Blende Magnesium Sulfide in Rechargeable Magnesium-Sulfur Batteries. *Chemistry of Materials* **2018,** *30* (18), 6318-6324.
36. Karakalos, S.; Siokou, A.; Ladas, S., The interfacial properties of MgCl2 films grown on a flat SiO2/Si substrate. An XPS and ISS study. *Applied Surface Science* **2009,** *255* (21), 8941-8946.
37. Araujo, J. R.; Archanjo, B. S.; de Souza, K. R.; Kwapinski, W.; Falcão, N. P. S.; Novotny, E. H.; Achete, C. A., Selective extraction of humic acids from an anthropogenic Amazonian dark earth and from a chemically oxidized charcoal. *Biology and Fertility of Soils* **2014,** *50* (8), 1223-1232.
38. Gao, T.; Hou, S.; Huynh, K.; Wang, F.; Eidson, N.; Fan, X.; Han, F.; Luo, C.; Mao, M.; Li, X.; Wang, C., Existence of Solid Electrolyte Interphase in Mg Batteries: Mg/S Chemistry as an Example. *ACS applied materials & interfaces* **2018,** *10* (17), 14767-14776.
39. Gursu, H., Preparation of Sulphur-Doped Graphene-Based Electrodes by Cyclic Voltammetry: A Potential Application for Vanadium Redox Flow Battery. *International Journal of Electrochemical Science* **2018**, 875-885.
40. Dedryvere, R.; Leroy, S.; Martinez, H.; Blanchard, F.; Lemordant, D.; Gonbeau, D., XPS valence characterization of lithium salts as a tool to study electrode/electrolyte interfaces of Li-ion batteries. *Journal of Physical Chemistry B* **2006,** *110* (26), 12986-12992.
41. Yuan, S.; Xiong, G.; He, F.; Jiang, W.; Liang, B.; Choong, C., Multifunctional REDV-conjugated zwitterionic polycarboxybetaine–polycaprolactone hybrid surfaces for enhanced antibacterial activity, anti-thrombogenicity and endothelial cell proliferation. *Journal of Materials Chemistry B* **2015,** *3* (41), 8088-8101.
42. Zhao, C.; Yan, Q.; Wang, S.; Dong, P.; Zhang, L., Regenerable g-C3N4–chitosan beads with enhanced photocatalytic activity and stability. *RSC Advances* **2018,** *8* (48), 27516-27524.
43. Hubert, J.; Poleunis, C.; Delcorte, A.; Laha, P.; Bossert, J.; Lambeets, S.; Ozkan, A.; Bertrand, P.; Terryn, H.; Reniers, F., Plasma polymerization of C4Cl6 and C2H2Cl4 at atmospheric pressure. *Polymer* **2013,** *54* (16), 4085-4092.
44. Kim, J.; Weber, I.; Buchner, F.; Schnaidt, J.; Behm, R. J., Surface chemistry and electrochemistry of an ionic liquid and lithium on Li4Ti5O12(111)-A model study of the anode|electrolyte interface. *J Chem Phys* **2019,** *151* (13), 134704.
45. Nitrogen Charge Distributions in Free-Base Porphyrins, Metalloporphyrins, and Their Reduced Analogues Observed by X-Ray Photoelectron Spectroscopy. *Inorganic Chemistry* **1976,** *15*.
46. Li, B.; Masse, R.; Liu, C.; Hu, Y.; Li, W.; Zhang, G.; Cao, G., Kinetic surface control for improved magnesium-electrolyte interfaces for magnesium ion batteries. *Energy Storage Materials* **2019,** *22*, 96-104.
47. Luo, J.; Xia, Y.; Zhang, J.; Guan, X.; Lv, R., Enabling Mg metal anodes rechargeable in conventional electrolytes by fast ionic transport interphase. *National Science Review* **2020,** *7* (2), 333-341.
48. Zhang, J.; Guan, X.; Lv, R.; Wang, D.; Liu, P.; Luo, J., Rechargeable Mg metal batteries enabled by a protection layer formed in vivo. *Energy Storage Materials* **2020,** *26*, 408-413.
49. Bhaghavathi Parambath, V.; Zhao-Karger, Z.; Diemant, T.; Jäckle, M.; Li, Z.; Scherer, T.; Gross, A.; Behm, R. J.; Fichtner, M., Investigation on the formation of Mg metal anode/electrolyte interfaces in Mg/S batteries with electrolyte additives. *Journal of Materials Chemistry A* **2020,** *8* (43), 22998-23010.
50. Rong, Z.; Malik, R.; Canepa, P.; Sai Gautam, G.; Liu, M.; Jain, A.; Persson, K.; Ceder, G., Materials Design Rules for Multivalent Ion Mobility in Intercalation Structures. *Chemistry of*

Materials **2015,** *27* (17), 6016-6021.
51. Frati, F.; Hunault, M.; de Groot, F. M. F., Oxygen K-edge X-ray Absorption Spectra. *Chemical reviews* **2020,** *120* (9), 4056-4110.
52. Luches, P.; D'Addato, S.; Valeri, S.; Groppo, E.; Prestipino, C.; Lamberti, C.; Boscherini, F., X-ray absorption study at the Mg and O K edges of ultrathin MgO epilayers on Ag(001). *Physical Review B* **2004,** *69* (4).
53. Nakanishi, K.; Ohta, T., Verification of the FEFF simulations to K-edge XANES spectra of the third row elements. *J Phys Condens Matter* **2009,** *21* (10), 104214.
54. Ogawa, S.; Murakami, S.; Shirai, K.; Nakanishi, K.; Ohta, T.; Yagi, S., NEXAFS Study of Air Oxidation for Mg Nanoparticle Thin Film. *Journal of Physics: Conference Series* **2013,** *417*, 012065.
55. Sharma †, R.; McKelvy, M. J.; Béarat, H.; Chizmeshya, A. V. G.; Carpenter, R. W., In-situnanoscale observations of the Mg(OH)2dehydroxylation and rehydroxylation mechanisms. *Philosophical Magazine* **2004,** *84* (25-26), 2711-2729.
56. Yogi, C.; Takamatsu, D.; Yamanaka, K.; Arai, H.; Uchimoto, Y.; Kojima, K.; Watanabe, I.; Ohta, T.; Ogumi, Z., Soft X-ray absorption spectroscopic studies with different probing depths: Effect of an electrolyte additive on electrode surfaces. *Journal of Power Sources* **2014,** *248*, 994-999.
57. Mangolini, F.; McClimon, J. B.; Rose, F.; Carpick, R. W., Accounting for nanometer-thick adventitious carbon contamination in X-ray absorption spectra of carbon-based materials. *Anal Chem* **2014,** *86* (24), 12258-65.
58. Wang, H.; Wu, C. H.; Weatherup, R. S.; Feng, B.; Ye, Y.; Liu, Y. S.; Glans, P. A.; Guo, J.; Fang, H. T.; Salmeron, M. B., X-ray-Induced Fragmentation of Imidazolium-Based Ionic Liquids Studied by Soft X-ray Absorption Spectroscopy. *The journal of physical chemistry letters* **2018,** *9* (4), 785-790.

TOC Figure